Delft University of Technology

Hybrid Additive Manufacturing of a Dielectric Resonator Phased Array Antenna at K Band

Hehenberger, Simon P.; Adithyababu, Aparna P.T.; Caizzone, Stefano; Aslan, Yanki; Yarovoy, Alexander

DOI
10.1109/ARRAY58370.2024.10880394

Publication date
2024

Document Version
Final published version

Published in
2024 IEEE International Symposium on Phased Array Systems and Technology, ARRAY 2024

Citation (APA)
Hehenberger, S. P., Adithyababu, A. P. T., Caizzone, S., Aslan, Y., & Yarovoy, A. (2024). Hybrid Additive Manufacturing of a Dielectric Resonator Phased Array Antenna at K Band. In *2024 IEEE International Symposium on Phased Array Systems and Technology, ARRAY 2024* (IEEE International Symposium on Phased Array Systems and Technology). IEEE. https://doi.org/10.1109/ARRAY58370.2024.10880394

Important note
To cite this publication, please use the final published version (if applicable).
Please check the document version above.

Copyright
Other than for strictly personal use, it is not permitted to download, forward or distribute the text or part of it, without the consent of the author(s) and/or copyright holder(s), unless the work is under an open content license such as Creative Commons.

Takedown policy
Please contact us and provide details if you believe this document breaches copyrights.
We will remove access to the work immediately and investigate your claim.

This work is downloaded from Delft University of Technology.
For technical reasons the number of authors shown on this cover page is limited to a maximum of 10.

Green Open Access added to TU Delft Institutional Repository

'You share, we take care!' - Taverne project

https://www.openaccess.nl/en/you-share-we-take-care

Otherwise as indicated in the copyright section: the publisher
is the copyright holder of this work and the author uses the
Dutch legislation to make this work public.

2024 IEEE International Symposium on Phased Array Systems and Technology (ARRAY) | 979-8-3503-9214-2/24/$31.00 ©2024 IEEE | DOI: 10.1109/ARRAY58370.2024.10880394

Hybrid Additive Manufacturing of a Dielectric Resonator Phased Array Antenna at K Band

Simon P. Hehenberger*, Aparna P. T. Adithyababu*, Stefano Caizzone*,Yanki Aslan† and Alexander Yarovoy†
*Institute of Communications and Navigation, German Aerospace Center, Wessling, Germany
Email: simon.hehenberger@dlr.de
†Microwave Sensing, Signals and Systems, Delft University of Technology, Delft, Netherlands

***Abstract*—This study explores the feasibility of using a hybrid additive manufacturing (AM) to design and produce low-cost, wideband phased array antennas for SatCom applications. We demonstrate the design, fabrication and experimental verification of an eight-element linear array comprised of multi-mode dielectric resonator antennas (DRAs) providing full coverage of the K-band SatCom downlink bandwidth (17.7-21.2 GHz). The impact of print settings on material properties is assessed and incorporated into the antenna design process. The manufactured prototype is experimentally verified via impedance and far-field measurements. Furthermore, beam steering capabilities are demonstrated using a commercially available integrated circuit and a simple calibration procedure. The phased array antenna achieves full coverage of the intended band with an input reflection coefficient below -10 dB. The averaged embedded element pattern demonstrates a realized gain of approximately 3 dB and a half-power beamwidth of 81 degrees. These results highlight the potential of combining hybrid AM and DRA technologies for future mmWave phased array development.**

***Index Terms*—Additive Manufacturing, SatCom, Dielectric Resonator Antenna, Phased Array, mmWave**

I. INTRODUCTION

Modern mmWave phased array antennas face challenges in providing sufficient bandwidth at a cost suitable for mass-market applications. Over the past decade, additive manufacturing (AM) has gained traction in radio frequency (RF) and microwave applications, enabling complex geometries and rapid prototyping [1], [2]. AM has been successfully applied to produce single-material conductive and dielectric components, such as dielectric resonator antennas (DRA) with engineered permittivity [3], [4], graded index lenses [5], horn antennas [6], slotted waveguide antennas [7], and metallic lens designs [8]. The primary utilized advantage of AM so far is its capability to engineer the effective dielectric permittivity of materials via non-resonant periodic structures, providing additional degrees of freedom in the design of novel RF and microwave devices.

However, single-material AM processes face limitations when developing advanced designs requiring multiple dielectrics and conductive materials or interfacing with conventional microwave equipment. Hybrid techniques, such as electroplating of printed parts [9] and copper foil deposition [10], can retain bulk metal conductivity but often require extensive postprocessing, limiting their ability to fully exploit AM's potential.

979-8-3503-9214-2/24/$31.00 ©2024 IEEE

Recently, AM technology has matured sufficiently to allow the combination of dielectric and conductive materials within the same process. Techniques like inkjet printing of dielectric and conductive inks [11], and the combination of extrusion-type AM with microdispensing of conductive inks [12], are particularly promising. While inkjet printing offers exceptional accuracy, extrusion-based methods are more accessible and compatible with a wide range of materials. Both methods trade bulk metal conductivity for the ability to manufacture complex parts in a single process, enabling the integration of dielectric materials with internal conductive traces or patches. This capability opens up tremendous possibilities in the design and manufacturing of novel antennas and complex metamaterial structures.

Extrusion-based hybrid AM has been used to create various antenna designs and RF components [13]–[15], though most applications have been limited to sub-10GHz frequencies and largely replicate designs already feasible with traditional methods. Regarding the utilization of AM for antenna applications, dielectric resonator antennas (DRAs) have emerged as a promising technology in the past decade, offering greater bandwidth and design flexibility for microwave and mmWave antennas compared to traditional microstrip patch antennas [17], [18]. The combination of hybrid AM and DRAs holds significant potential for developing low-cost, high-performance mmWave phased array antennas, yet this potential remains largely unexplored.

In this work, we demonstrate the feasibility of using hybrid AM and DRA technology to create wideband, low-cost phased array antennas for K-band receivers, covering the SatCom downlink band from 17.7 to 21.2 GHz. We introduce a novel DRA element design that utilizes two higher-order modes to achieve the desired bandwidth while enhancing directivity across the band. Additionally, we demonstrate the antenna's performance in an eight-element linear array configuration and its beam steering capabilities using a commercially available integrated circuit. The manufacturing process incorporates several innovative AM techniques: the DRA is printed using both low- and high-permittivity materials, with the high-permittivity material forming a periodic lattice to engineer the DRA's permittivity, and the low-permittivity material providing structural support. The ground plane and feedlines are fabricated using a low-loss dielectric and highly conductive silver ink. We also discuss the impact of print settings on material properties and

Authorized licensed use limited to: TU Delft Library. Downloaded on May 07,2025 at 08:06:14 UTC from IEEE Xplore. Restrictions apply.

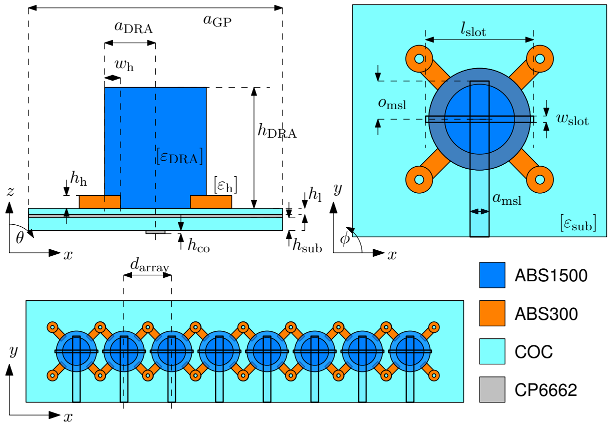

Fig. 1. Schematic drawing of the dielectric resonator antenna element considered in this work and its extension to an eight element linear array with color-coding corresponding to the different utilized materials.

experimentally characterize these effects to ensure accurate antenna performance prediction through full-wave simulations.

The remainder of this article is structured as follows: Section II details the antenna design, both standalone and within the linear array. Section III discusses the manufacturing setup and print settings, including inspection of the manufactured parts and identification of print artifacts. Section IV presents the experimental verification of the antenna in both standalone and array configurations through impedance and far-field measurements. Furthermore, beam steering with an eight-channel integrated circuit is demonstrated. Finally, Section V discusses the measurement results, and Section VI concludes the work.

II. DESIGN

A. Single Element Design

A schematic drawing of the proposed antenna is depicted in Figure 1. The design process and individual steps are explained in detail below.

1) Design methodology: While DRAs reportedly exhibit larger bandwidths than traditionally employed microstrip patch antennas, their bandwidth is insufficient to cover the whole SatCom downlink band in the K band ($17.7 - 21.2\text{GHz}$). To address this, we employed a technique that places two resonant modes in close frequency proximity, resulting in overlapping radiating bands and thus a wider bandwidth [19]. The antenna design process is carried out as follows.

(i) *Material Parameter Simulation:* We first identify the appropriate lattice constant and crystal symmetry for the DRA body, selecting a lower effective permittivity to reduce the Q factors of the resonant modes.

(ii) *Eigenmode Simulation:* Using CST's eigenmode solver, we determine the DRA dimensions (a_{DRA} and h_{DRA}) that support the selected modes at the desired resonant frequencies.

(iii) *Full-Wave Simulation:* Finally, we conduct full-wave simulations including the feed network to optimize the aperture dimensions and microstrip line termination, ensuring the antenna is well-matched.

2) Engineering the DRA permittivity: Given the available materials, the DRA is manufactured from high-permittivity ABS1500 thermoplastic, with a nominal permittivity of $\varepsilon_{\text{r, ABS1500}} = 15$ and a loss tangent of $\tan_\delta = 1.8\text{E}{-3}$. Although high-permittivity materials are a great tool to achieve miniaturization, they also limit the bandwidth of the resulting antenna. The capability of AM to create complex structures is commonly exploited to engineer the permittivity of some dielectric material by manufacturing a periodic structure with a given volumetric infill. Here we utilize dielectric periodic structures, or dielectric crystals, created via the superposition of spatial harmonics as introduced and demonstrated in [20] [21] to lower the DRAs effective permittivity to some desired value. Generally, there are two issues when engineering effective material parameters via AM periodic structures.

(i) *Printing Imperfections:* These introduce tiny air gaps, reducing permittivity [23] and causing effective uniaxial anisotropy due to the layer-by-layer construction [24].

(ii) *Frequency Dispersion:* Effective material parameters of periodic structures are inherently frequency-dispersive; thus, the lattice constant must be small enough to minimize this effect.

Both of these issues need to be taken into account for a successful design. The effective permittivity tensor of a solid part printed from the ABS1500 material with an extrusion width of 0.15mm and a layer height of 0.1mm is measured to be

$$[\varepsilon_{\text{r,ABS1500}}] = \begin{bmatrix} 13.36 & 0 & 0 \\ 0 & 13.32 & 0 \\ 0 & 0 & 11.71 \end{bmatrix}. \tag{1}$$

which is now assumed to be the permittivity of the host material for manufacturing the DRA. We select a face-centered-cubic (FCC) symmetry for the dielectric crystal, as it offers lower dispersion across a larger frequency band [22]. Several FCC unit cells, created with the spatial harmonic superposition method, with lattice constant a and different threshold values th, are depicted in Figures 2a-2c. The relationship between the threshold value and the volumetric infill fraction is depicted in Figure 2d. The effective material parameters are extracted via Floquet port scattering simulations as presented in [22]. The effective permittivity tensor components in non-dispersive frequency regimes are presented as a function of volumetric infill in Figure 2e, and the effective permittivity tensor components as a function of frequency for different lattice constants and a specific volumetric infill are depicted in Figure 2f. In order to avoid significant dispersion for frequencies up to 30GHz, a lattice constant $a = 1.5\text{mm}$ is selected for the further design. Although the permittivity tensor of the resonating body can be a powerful degree of freedom in the design of DRAs, as demonstrated in [25], the utilization of it is out of scope for this work. In this work, we specify the threshold of our periodic structure as 0.5, which provides a permittivity tensor for the DRA

$$[\varepsilon_{\text{r,DRA}}] = \begin{bmatrix} 5.5 & 0 & 0 \\ 0 & 5.5 & 0 \\ 0 & 0 & 5.1 \end{bmatrix}. \tag{2}$$

Authorized licensed use limited to: TU Delft Library. Downloaded on May 07,2025 at 08:06:14 UTC from IEEE Xplore. Restrictions apply.

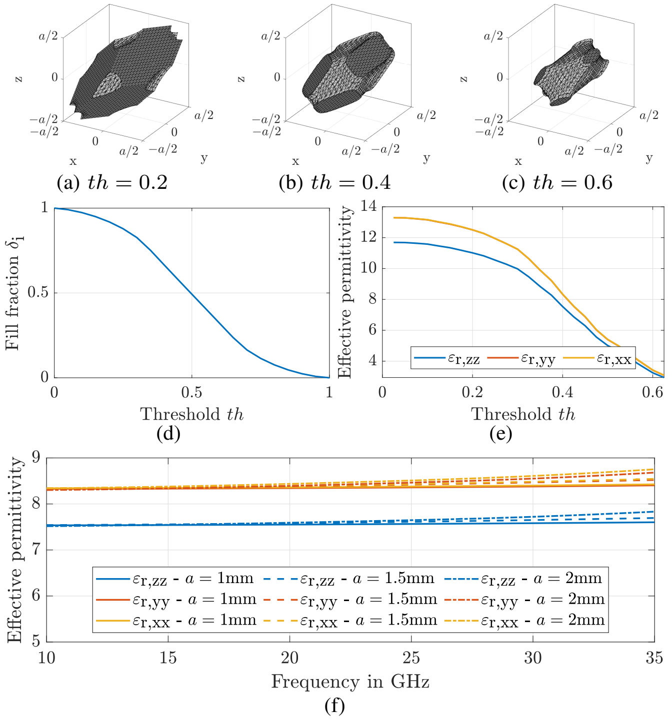

(a) $th = 0.2$ (b) $th = 0.4$ (c) $th = 0.6$

(d) (e)

(f)

Fig. 2. Unit-cells created via a threshold parameter th based on superimposed spatial harmonics in the direction of the reciprocal lattice vectors of the FCC crystal geometry, as defined in [21], and corresponding material parameter simulation results. (a) $th = 0.2$; (b) $th = 0.4$; (c) $th = 0.6$. The faces touching the boundaries of the crystal unit cell are shaded darker than faces that do not. (d) Relationship between the volumetric infill fraction and the threshold th parameter. Reprinted from [4]. (e) Tensor components as a function of frequency for different lattice constants a for threshold $th = 0.4$. (f) Tensor components as a function of spatial harmonic threshold.

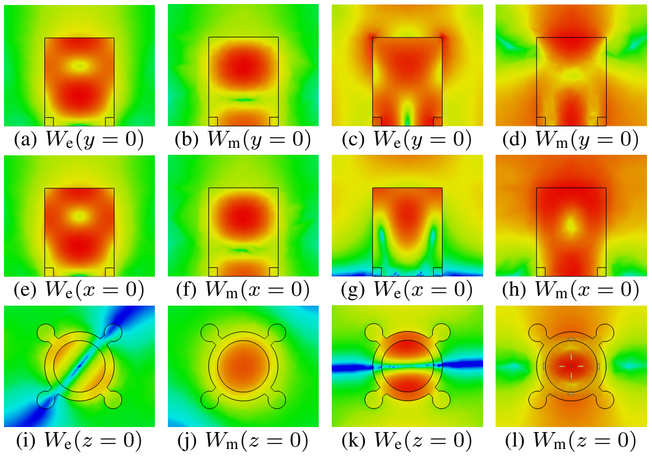

(a) $W_\text{e}(y=0)$ (b) $W_\text{m}(y=0)$ (c) $W_\text{e}(y=0)$ (d) $W_\text{m}(y=0)$

(e) $W_\text{e}(x=0)$ (f) $W_\text{m}(x=0)$ (g) $W_\text{e}(x=0)$ (h) $W_\text{m}(x=0)$

(i) $W_\text{e}(z=0)$ (j) $W_\text{m}(z=0)$ (k) $W_\text{e}(z=0)$ (l) $W_\text{m}(z=0)$

Fig. 3. Simulated electric (column 1 and 3) and magnetic (column 2 and 4) energy densities of the $HEM_{11\delta}$ (a,b,e,f,i,j) and $HEM_{12\delta}$ (c,d,g,h,k,l) in the xz- (row 1), yz- (row 2) and xy(z=0)- (row 3) planes.

3) DRA dimensions: In contrast to most DRA applications, we do not utilize the fundamental mode of the DRA, which usually provides a relatively broad beam, but rather opt for higher-order modes to increase the directivity of the antenna. Two different resonating DRA modes in close proximity are used to widen the bandwidth of the antenna. To this end, the $HEM_{11\delta}$ and $HEM_{12\delta}$ modes are selected, which both offer broadside radiation and relatively low Q factors. Furthermore, they both are compatible with feeding from a rectangular aperture in the ground plane due to the magnetic field distribution at the bottom of the DRAs. The DRA with permittivity tensor according to equation (2) is modeled together with the holding structure, as depicted in Figure 1, with parameters $w_\text{h} = 0.8\text{mm}$ and $h_\text{h} = 0.8\text{mm}$ in a CST eigenmode environment. The holding structure is printed from the ABS300 material from Avient which exhibits a nominal permittivity of $\varepsilon_{\text{r, ABS300}} = 3$ and a loss tangent of $\tan_\delta = 4.6\text{E}{-3}$. In the simulation the measured permittivity value of the ABS300 material, as reported in Section IV in equation (3), is utilized to model the holding structure. For DRA dimensions reported in Table I the desired modes exhibit resonance frequencies at 17.87 and 21.01GHz with corresponding Q factors 9.3 and 3.2, respectively. The electric W_e and magnetic W_m energy densities of the selected modes are depicted in Figure 3 in the $xz(y=0)$-, $yz(x=0)$- and $xy(z=0)$-planes respectively.

4) Element feed: The antenna is excited using a 50Ω microstrip transmission line on a substrate with height h_sub made from Cyclo-Olefin-Copolymer (COC) from Creamelt, a low-permittivity ($\varepsilon_{\text{r,COC}} = 2.4$), low-loss ($\tan_\delta = 2\text{E}{-4}$) material thermoplastic. The antenna and transmission line are coupled via a rectangular aperture directly below the dielectric resonator with dimensions l_slot and w_slot. The transmission line is terminated with an open at an offset of o_msl w.r.t. the center of the slot. The DRA is positioned centrally above the feed aperture and fixed in place via four M2 nylon screws. Since printing conductive ink directly to the heated print bed is not possible, an additional layer of substrate with height h_l between the ground plane and the DRA is considered in the design. For later manufacturing, a layer height of 0.12mm is selected for the feed substrate. It is desired to extrude two and four layers for the spacer substrate and microstrip substrate, respectively, resulting in $h_\text{l} = 0.24\text{mm}$ and $h_\text{sub} = 0.48\text{mm}$. The microstrip substrate exhibits a permittivity of $\varepsilon_{\text{r,sub}} = \varepsilon_{\text{r,COC}}$, as reported in (4) in Section IV, and the conductive ink is dispensed with 0.04mm layer height, which implies a line width of $a_\text{msl} = 1.5\text{mm}$ to realize a characteristic impedance of $Z_0 = 50\Omega$. The remaining parameters of the feed structure, namely the rectangular aperture dimensions l_slot and w_slot as well as the microstrip termination offset o_msl, are subject to an optimization routine in a full-wave simulation environment with the goal to minimize the input reflection coefficient at the resonance frequencies obtained via the eigenmode simulation explained above. The input reflection coefficient as a function of frequency and the co- and cross-polar far-field plots are depicted in Figure 6. The local minima of the input reflection coefficient at 17.7 and 21.4 GHz correspond well to the predicted values from the eigenmode simulation. The full-wave simulations show realized gain values of 9.06 dB and 7.6 dB for $\theta = 0$, at the two resonance frequencies respectively. All geometric parameters are summarized in Table I.

Authorized licensed use limited to: TU Delft Library. Downloaded on May 07,2025 at 08:06:14 UTC from IEEE Xplore. Restrictions apply.

TABLE I
GEOMETRIC PARAMETERS OF PROPOSED DIELECTRIC RESONATOR ANTENNA DESIGN.

Variable	**Value**	**Variable**	**Value**
a_{DRA}	3.15 mm	h_{DRA}	8 mm
a_{GP}	50 mm	h_{sub}	0.48 mm
w_{h}	0.8 mm	h_{h}	0.8 mm
a_{msl}	1.5 mm	o_{msl}	3.5 mm
l_{slot}	7 mm	w_{slot}	0.45 mm
h_{l}	0.24 mm	h_{co}	40 µm

TABLE II
HARDWARE CONFIGURATION OF THE TOOLCHANGER ADDITIVE MANUFACTURING SETUP.

E3D Motion System - Toolchanger Configuration				
Tool	**1**	**2**	**3**	**4**
Device	E3D Hemera Extruder	E3D Hemera Extruder	ViscoTec vipro-HEAD 3	E3D Hemera Extruder
Material	Avient ABS1500	Avient ABS300	Elantas Bectron CP6662	Creamelt COC
Orifice diameter	0.15mm	0.15mm	0.2mm	0.6mm

B. Array

The designed element, without further optimization is introduced into the eight element linear array geometry with a half-wavelength spacing at 19 GHz corresponding to an inter-element distance, as indicated in Figure 1, of $d_{\text{array}} = 7.9\text{mm}$. The arm-length of the holding structure is chosen such that the mounting holes of neighboring elements coincide.

III. MANUFACTURING

A. Hardware Setup and Print Parameters

The manufacturing setup is based on a *core-XY* tool changing concept based on the E3D motion system platform equipped with four independent tools that can be switched during the print process, allowing for flexible multi-material printing. In our case, the system is equipped with three E3D Hemera filament extruders for the three utilized dielectrics and a third-party printhead, Vipro-HEAD 3 from VisoTec GmbH, for silver ink dispensing. The ViproHead printhead is selected due to its precise dispensing capabilities and stepper motor interface, which allows straightforward integration into the existing print hardware. The hardware setup is summarized in Table II, and the corresponding print settings are reported in Table III.

B. RF interface

In order to support measurements of the manufactured antennas, an interface from the microstrip feed network to the measurement equipment needs to be established. In this work, we utilize a 2.92mm SMA connector (Amphenol SF1521-60061) that is screwed onto the substrate and establishes a reliable connection via compression. The choice of the connector is driven by the necessity to employ a low-temperature solution because the utilized substrate material has a comparably low glass-transition temperature of $80°\text{C}$, which renders it incompatible with soldering techniques.

TABLE III
MATERIAL PRINT SETTINGS

Setting - Material	**ABS1500**	**ABS300**	**CP6662**	**COC**
Extrusion width [mm]	0.15	0.15	0.2	0.6
Nozzle temp. [°C]	280	230	-	245
Bed temp. [°C]	105	105	55	75
Max. speed $[\mathrm{mm\,s^{-1}}]$	5	7.5	10	60
Max. acc. $[\mathrm{mm\,s^{-2}}]$	200	200	100	1500
Layer height [mm]	0.1	0.1	0.04	0.12

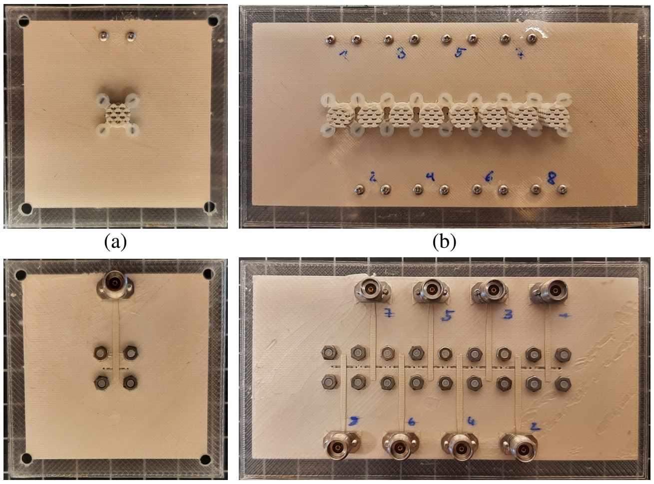

(a) (b)
(c) (d)

Fig. 4. Manufactured prototypes of the K band DRA antennas, manufactured via hybrid additive techniques. Single element (a) front, (c) back. Eight element linear array (b) front, (d) back.

C. Visual inspection

Figure 4 depicts the manufactured single element and array antennas with mounted connectors. To provide sufficient space for the connectors, the feedlines of odd-numbered elements in the array are flipped around to the other side of the substrate, as opposed to the depiction in Figure 1. Although the print can be considered successful, several imperfections can be identified in the prints and are studied further in detail below.

1) Air gaps and warping in extruded dielectrics: Air gaps and layer lines can be seen in the dielectric parts in Figure 5. This effect has already been explained above in Section II-2 and is most obvious in the substrate material COC due to the large nozzle utilized during the print and the transparent nature of the thermoplastic. Furthermore, the ABS materials are prone to warping due to temperature differences in the material during manufacturing, which may result in slightly twisted geometries, as can be observed on the holding structure in Figure 5b.

2) Ink dispensing edges: The dispensing of silver ink onto the substrate material does not create perfect edges, as depicted in Figures 5c; this results in small variations in the thickness of the microstrip lines and a blurring of the edges

Authorized licensed use limited to: TU Delft Library. Downloaded on May 07,2025 at 08:06:14 UTC from IEEE Xplore. Restrictions apply.

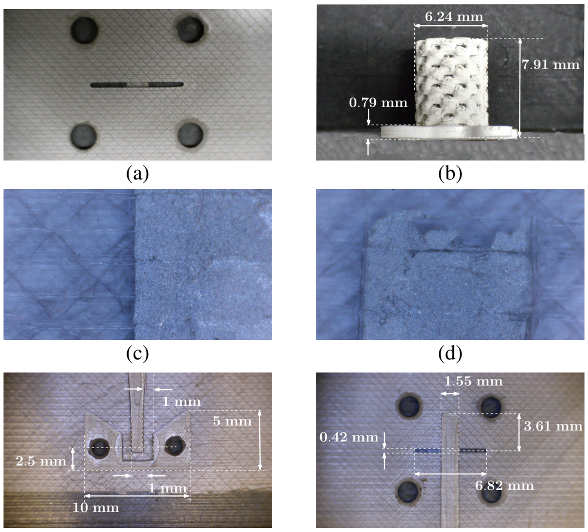

(a) (b)

(c) (d)

(e) (f)

Fig. 5. Visual inspection and identification of imperfections in the printed parts. (a) Gaps in the substrate material along the extruded lines and blurred corners of the rectangular slot. (b) Layer lines and 'blobs' of extruded materials on the DRA. (c) Microstrip line edge - blurry edge. (d) Microstrip line edge open termination - under extrusion. (e) Connector landing pad - dimensions. (f) Slot and microstrip line dimensions.

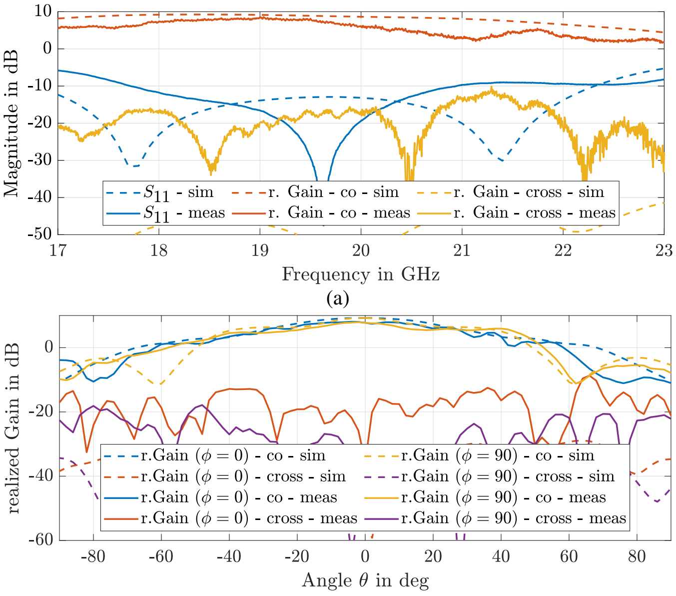

(a)

(b)

Fig. 6. Measurement results of the single element antenna prototype compared to simulation results. (a) Input reflection coefficient and realized gain in cross- and co-polarization as a function of frequency. (b) Co- and cross-polarized realized gain values at 19 GHz.

in the rectangular feed aperture. Furthermore, ink dispensing inconsistencies result in areas with no ink coverage, as can be observed in Figure 5d.

3) Dimensions of printed parts: The tolerances of the manufacturing lead to slightly different values for the microstrip line widths, offsets, and slot dimensions as depicted in 5e and 5f, respectively. Furthermore, the ABS materials from Avient are prone to shrinkage during part cooldown after the printing process, which results in slightly reduced dimensions of the printed parts as depicted in Figure 5b.

IV. SIMULATION AND MEASUREMENT RESULTS

A. Material Parameters

1) Dielectric properties: To achieve an accurate simulation of the antenna, the anisotropic permittivity of both the ABS1500, ABS300 and COC, printed with settings provided in Table III, are measured with a quadratic aperture waveguide system in the X-band as explained in [24], and the averaged real-valued[1] permittivity tensors are

$$[\varepsilon_{\mathrm{r,ABS300}}] = \begin{bmatrix} 2.95 & 0 & 0 \\ 0 & 2.95 & 0 \\ 0 & 0 & 2.86 \end{bmatrix} \tag{3}$$

and,

$$[\varepsilon_{\mathrm{r,COC}}] = \begin{bmatrix} 2.25 & 0 & 0 \\ 0 & 2.25 & 0 \\ 0 & 0 & 2.20 \end{bmatrix}. \tag{4}$$

The measured permittivity value for the ABS1500 material has already been reported above in equation (1). Measurements of the From the extracted material permittivity tensor values in (1), (3) and (4), we can see that the layer-by-layer buildup results in a uniaxial anisotropic material with negative birefringence [24].

2) Conductivity: After dispensing, the Bectron CP 6662 silver ink is thermally cured by pausing the print and setting the heated bed to the desired curing temperature (120 °C for 10 minutes). The surface resistivity ρ_{s} after thermal curing is measured with a four-point-probe system Jandel RM3-AR from Polytech GmbH to be about $\rho_{\mathrm{s}} = 12$ mΩ/sq for a layer height of 40µm, corresponding well to the value reported in the datasheet of the ink (10 mΩ/sq/mil).

B. Single Element

The single DRA element, as depicted in Figure 4, is characterized by input reflection coefficient and far-field radiation while being mounted in a benchtop anechoic chamber from Millibox. The input reflection coefficient and the co- and cross-polarized realized gain values obtained through measurement and full-wave simulation are compared in Figure 6a. Furthermore, the measured co- and cross-polarized realized gain patterns are displayed for orthogonal azimuth cuts for 19GHz in Figure 6b.

C. Embedded Element

The embedded elements are first measured in a passive configuration and then connected to the evaluation board of the Anokiwave AWMF-0197, a commercially available integrated circuit intended for satellite communication receivers operating in the desired frequency range. The mounting of the array together with the evaluation board is depicted in Figure 9.

---

[1] imaginary parts omitted for brevity sake

Authorized licensed use limited to: TU Delft Library. Downloaded on May 07,2025 at 08:06:14 UTC from IEEE Xplore. Restrictions apply.

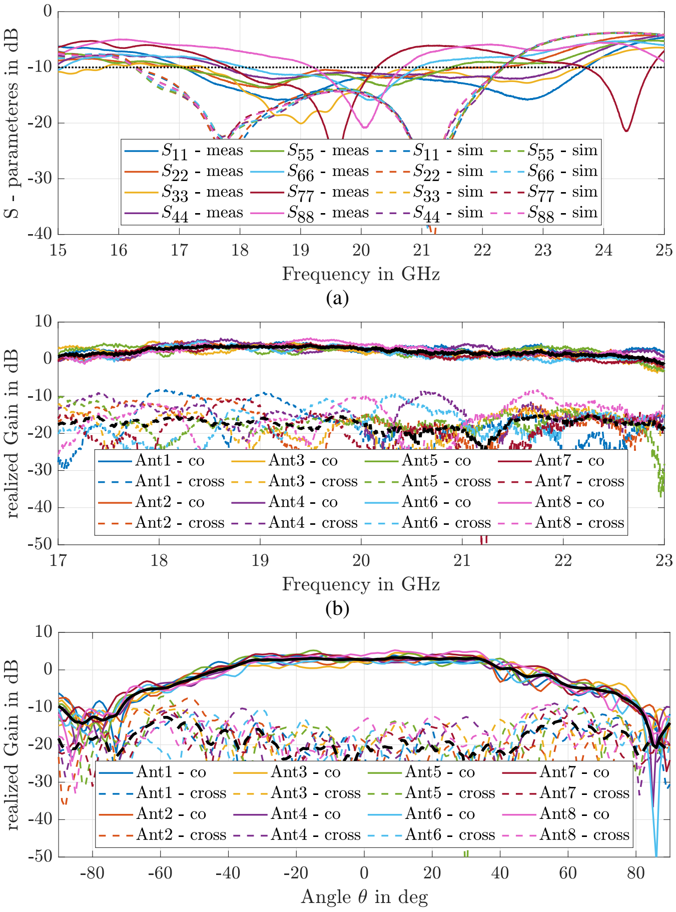

(a)

(b)

(c)

Fig. 7. Measurement results of the passive embedded elements. (a) Input reflection coefficients as a function of frequency compared to simulation results. (b) Cross- and co-polarized realized gain values of the individual elements at $\theta = 0$ as a function of frequency. (c) Cross- and co-polarized realized gain values of the individual embedded antenna elements as a function of the angle θ for two orthogonal azimuth cuts. Bold black curves correspond to the averaged beampattern values over all elements.

1) Passive: Embedded input reflection coefficient measurements of each array element are depicted in Figure 7a. Furthermore, the measured cross- and co-polarized realized gain is plotted as a function of frequency in Figure 7b and at 20 GHz as a function of the angle θ for two orthogonal azimuth cuts in Figure 7c. Additionally, measured values for the impedance bandwidth and half-power beam widths are reported in Table IV.

2) Active via Anokiwave AWMF 0197 IC: The measured cross- and co-polarized realized gain is plotted as a function of frequency in Figure 8a and at 20 GHz as a function of the angle θ for two orthogonal azimuth cuts in Figure 8b.

TABLE IV
IMPEDANCE BANDWIDTH AND HALF POWER (HP) BEAMWIDTH MEASUREMENT RESULTS OF THE SINGLE ELEMENT AND EMBEDDED ANTENNA ELEMENTS.

	Impedance Bandwidth			**HP beamwidth**		
	f_l GHz	f_u GHz	B GHz | %	θ_1 deg	θ_2 deg	θ_{HPBW} deg
Single Element	17.71	20.95	3.24 | 17.1	24	24	48
Ant. 1	17.06	23.72	6.66 | 35.1	−43	31	74
Ant. 2	17.13	22.13	5.00 | 26.3	−42	38	80
Ant. 3	17.40	23.59	6.20 | 32.6	−5	39	44
Ant. 4	17.71	23.34	5.62 | 29.6	−35	36	71
Ant. 5	17.01	21.48	4.47 | 23.5	−36	31	67
Ant. 6	18.09	20.93	3.00 | 15.8	−36	42	78
Ant. 7	17.84	20.26	2.42 | 12.7	−40	42	82
Ant. 8	19.20	20.69	1.49 | 7.8	−30	39	69
Avgd. Pattern	17.47	21.24	4.36 | 22.9	−41	40	81

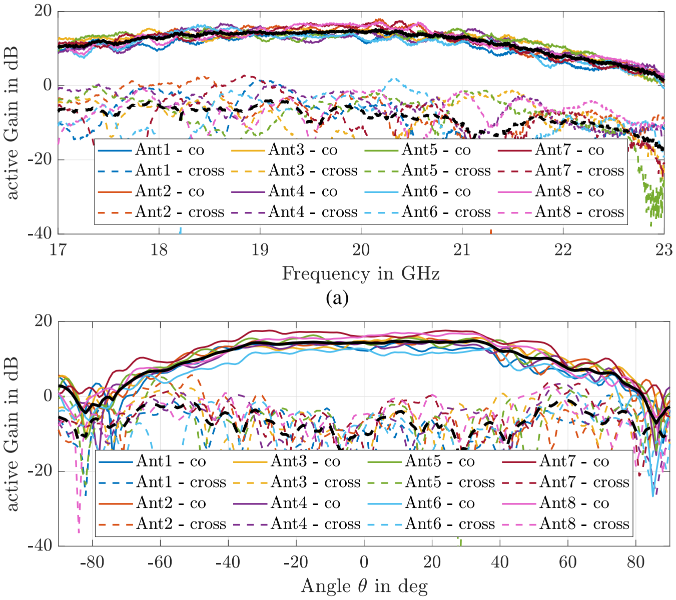

(a)

(b)

Fig. 8. Measurement results of the active embedded elements. (a) Cross- and co-polarized realized gain values of the individual elements at $\theta = 0$ as a function of frequency. (b) Cross- and co-polarized realized gain values of the individual embedded antenna elements as a function of the angle θ for two orthogonal azimuth cuts. Bold black curves correspond to the averaged beampattern values over all elements.

D. Array measurements

A beamforming measurement with a uniform excitation is carried out. Calibration weights for the individual channels of the Anokiwave IC are simply extracted from the embedded element measurements at $\theta = 0$ and 20 GHz. The IC provides five- and six-bit digital control for attenuation and phase, respectively, on each channel, implying a discretization error in the individual channel weights. Optimal and configured individual channel gain values and phase shifts are depicted in Figure 10a. Furthermore, Figures 10b and 10d depict the resulting combined beampattern measurements for steering angles 0° and 30° respectively.

V. DISCUSSION

A. Single element

The measurement results for the single element, presented in Figure 6, reveal a shift in the targeted mode resonance frequencies, indicated by two local minima in the measured

Authorized licensed use limited to: TU Delft Library. Downloaded on May 07,2025 at 08:06:14 UTC from IEEE Xplore. Restrictions apply.

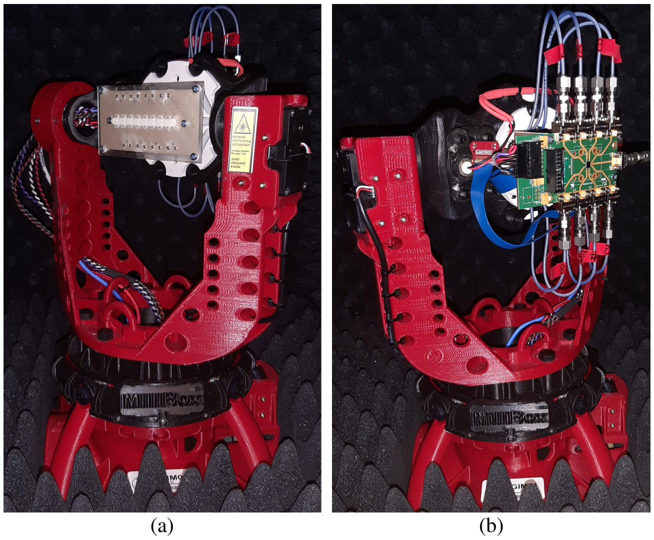

Fig. 9. The linear dielectric resonator phased array prototype is mounted on the Millibox positioner (a), with individual antenna elements connected to the inputs of the Anokiwave AWMF0197 beamformer IC (b).

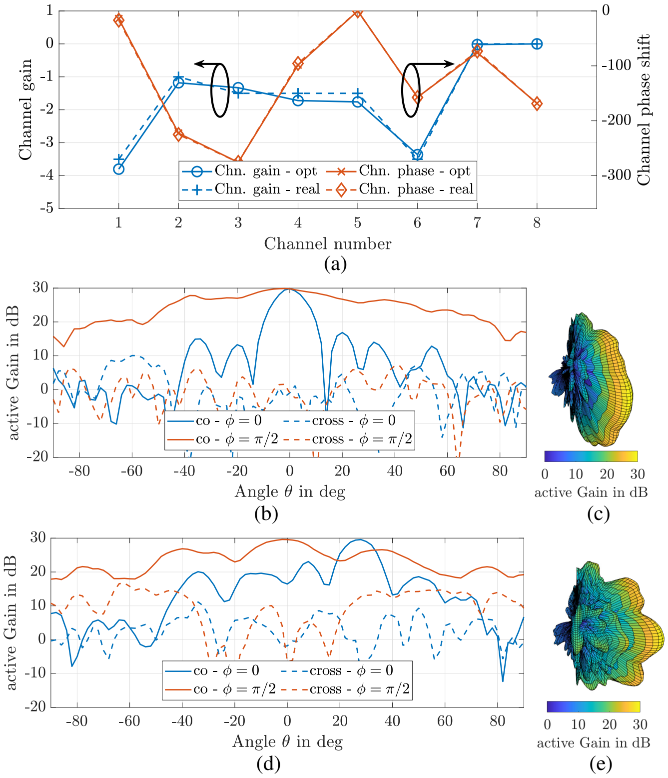

Fig. 10. Array measurement results. (a) Extracted attenuation and phase offset calibration values from individual embedded element measurements at $\theta = 0$ and 20 GHz. (b),(d) Co- and cross-polarized realized gain values of the uniformly excited antenna array steered to 0° and 30° respectively as a function of the angle θ. (c),(e) 3D active gain patterns of the uniformly excited antenna array steered to 0° and 30° respectively.

S_{11} parameter—one at approximately 19.5 GHz and another at approximately 22.5 GHz. While the match for the first resonance is excellent, the matching for the upper mode is slightly suboptimal. This resonance shift is likely caused by a slight under-extrusion during the printing of the DRA periodic structure, leading to a lower-than-targeted effective permittivity and, consequently, a shift to higher frequencies. This effect also impacts the feed network performance, which was optimized based on the targeted effective permittivity. Additionally, tolerances in the print process contribute to the observed deviations from the desired performance. The far-field results generally align well with the simulations, though increased deviations are noted at high θ angles, which can be attributed to interference from the millibox positioner at these angles. A slight reduction in realized gain, observed in Figure 6, is likely due to additional losses from the SMA connector, which were not accounted for in the simulations.

B. *Embedded elements*

The input reflection coefficient of the embedded elements, as shown in Figure 7, generally exhibits the same upward shift in resonances as observed with the single element. Notably, elements 7 and 8 show more significant deviations, with element 7 displaying a pronounced second resonance at approximately 24.5 GHz. For the purposes of this discussion, we focus on results at 20 GHz, where all elements exhibit an input reflection coefficient of less than -10 dB.

Realized gain values exhibit a mean of $\approx 3 \pm 1$dB in co- and $\approx -20 \pm 5$dB in cross-polarized components at $\theta = 0$, which is a significant reduction in the co-polarized component compared to the values obtained in the single element. The reason for the reduced gain at $\theta = 0$ is a broadening of the embedded beam pattern through mutual coupling compared to the single element from a half-power beamwidth (HPBW) of 48° in the single element to 82° in the averaged embedded pattern. Individual measured values of the impedance bandwidth and HPBW in Table IV show a degrading performance for array elements with increasing index in the array. Although this artifact might be a coincidence, it may also indicate a degradation of print performance on one side of the array due to an uneven print surface.

Similar results are obtained via the measurements where the individual antenna elements are connected to the input ports of the Anokiwave AWMF0197 evaluation board. The main difference is the increased element gain of $\approx 15.2 \pm 1.5$dB and corresponding variations due to the included low noise amplifier and internal channel differences.

C. *Beamforming*

While Figure 10a depicts the optimum calibration weights for uniform excitation at 20GHz, the Anokiwave AWMF0197 provides five- and six-bit digital control for attenuation and phase, respectively, on each individual channel which implies a non-optimal result for the combined antenna pattern. Nevertheless, the desired increase in directivity from combining the individual antenna elements as well the possibility of

Authorized licensed use limited to: TU Delft Library. Downloaded on May 07,2025 at 08:06:14 UTC from IEEE Xplore. Restrictions apply.

steering the beam can be observed in Figures 10b and 10d. The comparably high sidelobe level of $\approx -8\mathrm{dB}$ in Figure 10d is most likely due to the non-optimal calibration.

VI. CONCLUSION

This study demonstrates the feasibility of realizing K-band arrays for SatCom applications using low-cost additive manufacturing (AM) techniques. We designed and fabricated a multi-mode dielectric resonator phased array antenna using extrusion-based additive techniques combined with the dispensing of highly conductive silver particulate ink. The DRA design incorporates both high- and low-permittivity extruded thermoplastic materials to engineer the effective permittivity of the DRA while integrating it into a mechanically robust holding structure for easy installation on the feed substrate. The entire manufacturing process was achieved using a low-cost system based on off-the-shelf components. A low-loss dielectric material, along with dispensed silver ink, was used to create a planar network to excite the individual antenna elements via an aperture-coupled microstrip line.

This work also addresses the particularities and challenges associated with the employed AM techniques, such as the influence of print settings on material parameters, the inherent anisotropy of the extrusion process, and dispersion in periodic dielectric lattices.

The manufactured antenna is validated through impedance and far-field measurements in both standalone and embedded configurations. Additionally, beamforming is demonstrated using a dedicated integrated circuit and a simple calibration procedure. Despite some remaining manufacturing imperfections, the fabricated design closely matches simulated and required performance criteria.

While hybrid manufacturing technology still requires significant advancements to reliably produce K-band components, this work highlights the substantial potential of low-cost hybrid additive techniques for mmWave applications. The results suggest a promising future for these technologies in the development of advanced antenna systems.

REFERENCES

[1] E. S. Rosker, R. Sandhu, J. Hester, M. S. Goorsky, and J. Tice, ‘Printable materials for the realization of high performance RF components: Challenges and opportunities’, Int. J. Antennas Propag., vol. 2018, pp. 1–19, 2018.

[2] T. Whittaker, S. Zhang, A. Powell, C. J. Stevens, J. Y. C. Vardaxoglou, and W. Whittow, ‘3D Printing Materials and Techniques for Antennas and Metamaterials: A survey of the latest advances’, IEEE Antennas Propag. Mag., vol. 65, no. 3, pp. 10–20, Jun. 2023.

[3] Q. Lamotte et al., ‘Multi-permittivity 3D-printed ceramic dual-band circularly polarized dielectric resonator antenna for space applications’, in 2021 15th European Conference on Antennas and Propagation (EuCAP), Dusseldorf, Germany, 2021.

[4] S. P. Hehenberger, S. Caizzone, and A. G. Yarovoy, ‘Additive manufacturing of linear continuous permittivity profiles and their application to cylindrical dielectric resonator antennas’, IEEE Open J. Antennas Propag., vol. 4, pp. 373–382, 2023.

[5] J. W. Allen and B.-I. Wu, ‘Design and fabrication of an RF GRIN lens using 3D printing technology’, in Terahertz, RF, Millimeter, and Submillimeter-Wave Technology and Applications VI, San Francisco, California, USA, 2013.

[6] A. Sharma, R. K. Stilwell, S. Szczesniak, and C. Carpenter, ‘3D metal printed Ka-band quad-ridge horn antenna’, in 2022 IEEE International Symposium on Antennas and Propagation and USNC-URSI Radio Science Meeting (AP-S/URSI), Denver, CO, USA, 2022.

[7] T. Van Trinh, J. Park, C. M. Song, S. Song, and K. C. Hwang, ‘A 3-D metal-printed dual-polarized ridged waveguide slot array antenna for X-band applications’, Appl. Sci. (Basel), vol. 13, no. 8, p. 4996, Apr. 2023.

[8] D. Shamvedi, P. O’Leary, and R. Raghavendra, ‘Development of 3D printed metallic lenses’, in 2023 17th European Conference on Antennas and Propagation (EuCAP), Florence, Italy, 2023.

[9] D. Panusch, F. Hubert, F. Bachbauer, K. Lomakin, and G. Gold, ‘Additively manufactured helix antenna for X-band applications’, in 2022 16th European Conference on Antennas and Propagation (EuCAP), Madrid, Spain, 2022.

[10] X. Yu et al., ”3-D Printed Parts for a Multilayer Phased Array Antenna System,” in IEEE Antennas and Wireless Propagation Letters, vol. 17, no. 11, pp. 2150-2154, Nov. 2018.

[11] M. Li, Y. Yang, F. Iacopi, J. Nulman and S. Chappel-Ram, ”3D-Printed Low-Profile Single-Substrate Multi-Metal Layer Antennas and Array With Bandwidth Enhancement,” in IEEE Access, vol. 8, pp. 217370-217379, 2020.

[12] B.Niese, P. Amend, T. Frick, S. Roth and M. Schmidt, ”Fast and flexible production of mechatronic integrated devices by means of additive manufacturing,” 2016 12th International Congress Molded Interconnect Devices (MID), Wuerzburg, Germany, 2016.

[13] S. P. Hehenberger, S. Caizzone and A. Yarovoy, ”Low-Cost Hybrid Additive Manufacturing of a Miniaturized Dual Band Stacked Patch Antenna for GNSS Applications,” 2024 18th European Conference on Antennas and Propagation (EuCAP), Glasgow, United Kingdom, 2024.

[14] K. H. Church et al., ”Multimaterial and Multilayer Direct Digital Manufacturing of 3-D Structural Microwave Electronics,” in Proceedings of the IEEE, vol. 105, no. 4, pp. 688-701, April 2017.

[15] T. P. Ketterl et al., ”A 2.45 GHz Phased Array Antenna Unit Cell Fabricated Using 3-D Multi-Layer Direct Digital Manufacturing,” in IEEE Transactions on Microwave Theory and Techniques, vol. 63, no. 12, pp. 4382-4394, Dec. 2015

[16] J. Castro, E. Rojas, A. Ross, T. Weller and J. Wang, ”High-k and low-loss thermoplastic composites for Fused Deposition Modeling and their application to 3D-printed Ku-band antennas,” 2016 IEEE MTT-S International Microwave Symposium (IMS), San Francisco, CA, USA, 2016.

[17] S. Keyrouz and D. Caratelli, “Dielectric Resonator Antennas: Basic Concepts, Design Guidelines, and Recent Developments at Millimeter-Wave Frequencies,” International Journal of Antennas and Propagation, vol. 2016. Hindawi Limited, pp. 1–20, 2016.

[18] F. P. Chietera, R. Colella, and L. Catarinucci, “Dielectric Resonators Antennas Potential Unleashed by 3D Printing Technology: A Practical Application in the IoT Framework,” Electronics, vol. 11, no. 1. MDPI AG, p. 64, Dec. 26, 2021.

[19] N. A. Abd Rahman et al., “A Review of Circularly Polarized Dielectric Resonator Antennas: Recent Developments and Applications,” Micromachines, vol. 13, no. 12. MDPI AG, p. 2178, Dec. 08, 2022.

[20] R. C. Rumpf and J. Pazos, “Synthesis of spatially variant lattices,” Optics Express, vol. 20, no. 14. The Optical Society, p. 15263, Jun. 22, 2012.

[21] S. P. Hehenberger, A. P. T. Adithyababu, and S. Caizzone, “Effective Permittivity Measurement of 3D-Printed Dielectric Crystals,” 2022 16th European Conference on Antennas and Propagation (EuCAP). IEEE, Mar. 27, 2022.

[22] S. P. Hehenberger, S. Caizzone, S. Thurner, and A. G. Yarovoy, “Broadband Effective Permittivity Simulation and Measurement Techniques for 3-D-Printed Dielectric Crystals,” IEEE Transactions on Microwave Theory and Techniques, vol. 71, no. 10. Institute of Electrical and Electronics Engineers (IEEE), pp. 4161–4172, Oct. 2023.

[23] A. Goulas et al., ”The impact of 3D printing process parameters on the dielectric properties of high permittivity composites,” Designs, vol. 3, no. 4, p. 50, Nov. 2019

[24] S. P. Hehenberger et al., ‘Dielectric Anisotropy in Materials Manufactured via Fused Filament Fabrication Processes’, Material Research Bulletin (unpublished)

[25] S. Fakhte, H. Oraizi, L. Matekovits and G. Dassano, ”Cylindrical Anisotropic Dielectric Resonator Antenna With Improved Gain,” in IEEE Transactions on Antennas and Propagation, vol. 65, no. 3, pp. 1404-1409, March 2017.

Authorized licensed use limited to: TU Delft Library. Downloaded on May 07,2025 at 08:06:14 UTC from IEEE Xplore. Restrictions apply.